ORIGINAL PAPER: NANO-STRUCTURED MATERIALS (PARTICLES, FIBERS, COLLOIDS, COMPOSITES, ETC.)

Ag-Ni alloy nanoparticles decorated reduced graphene oxide nanocomposite as highly efficient recyclable catalyst for the reduction of 4-nitrophenol and methylene blue

Xing-Wei Han [ID][1] · Zhuoran Ma[1] · Juan Peng[1] · Huaqing Zhang[1] · Yang Yang[1] · Jianing Zhang[1] · Shuai Guo[1] · Huiying Pan[1]

Abstract

With L-ascorbic acid as reducing agent and GO as support, an in-situ co-reduction method was proposed for anchoring Ag-Ni alloy nanoparticles onto reduced graphene oxide (rGO) (Ag-Ni/rGO). Various of characterization instruments were utilized to characterize the morphology, structure, and composition of Ag-Ni/rGO. These characterization results revealed that Ag-Ni alloy nanoparticles with average diameter of 36.95 nm were homogeneously decorated on rGO sheets. The resultant Ag-Ni/rGO nanocomposite was highly active toward the reduction of 4-nitrophenol and methylene blue. The ferromagnetic nature of the as-prepared products makes them can be recycled and reused easily. It is believed that the enhancement of the catalytic performance is originated from the strong synergistic effect between Ag and Ni of Ag-Ni alloy nanoparticles along with enrichment of rGO to a great degree.

✉ Xing-Wei Han
   hanxingwei0529@sina.com

[1] School of Environmental and Chemical Engineering, Shenyang Ligong University, Shenyang 110159, China

Graphical Abstract
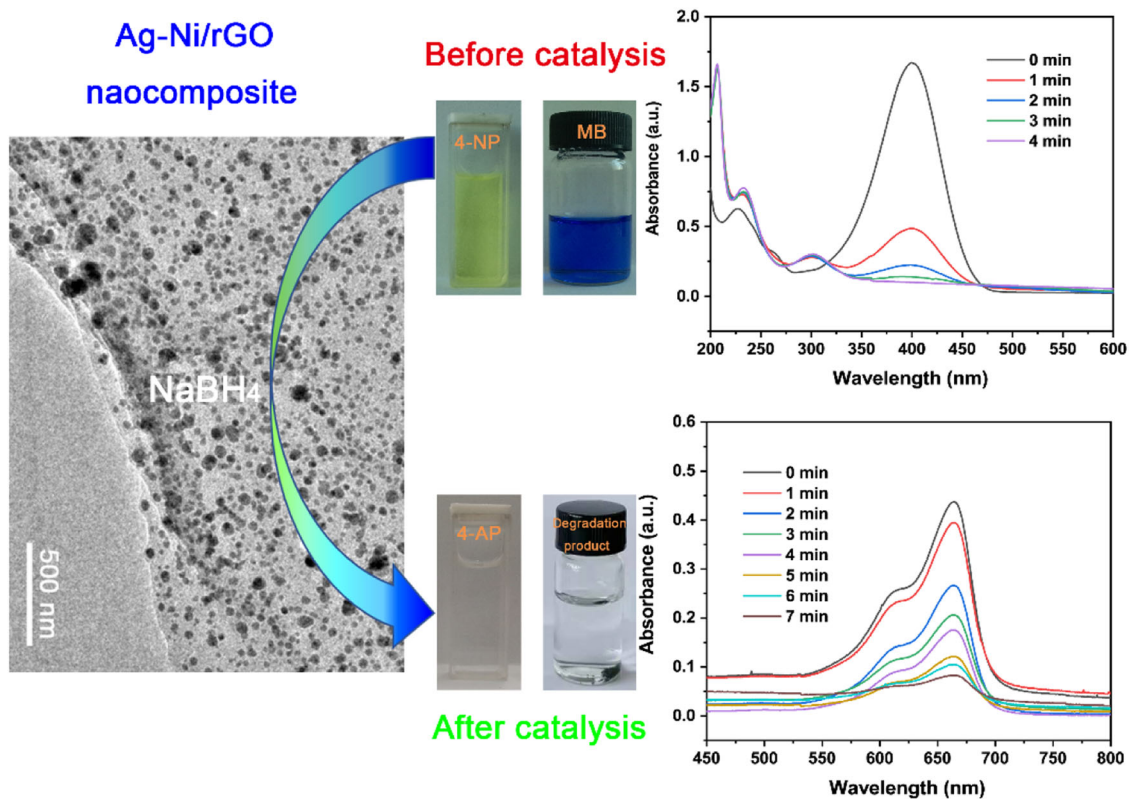
Keywords Ag-Ni alloy nanoparticles · Reduced graphene oxide · Catalysis · 4-nitrophenol · Methylene blue.

Highlights

- Ag-Ni/rGO nanocomposite was prepared via an in-situ co-reduction method.
- The Ag-Ni/rGO possesses outstanding catalytic activity for the reduction of 4-nitrophenol and methylene.
- The synergistic effect between Ag and Ni of Ag-Ni alloy nanoparticles along with the enrichment of rGO helped in enhancing the catalytic capacity of Ag-Ni/rGO.

1 Introduction

Environmental contamination, especially water contamination has captured widespread concern due to the rapid development of industries and the discharge of pollutants into aquatic system year by year [1, 2]. Dyes and nitroaromatic, important industrial raw materials and intermediates, are widely used in drugs, textile, cosmetic, paper, plastic, leather, and so on. Meanwhile, they are notorious water pollutants for their toxicity, carcinogenicity, and mutagenicity which will cause damage to the liver, kidney, and central nervous system of human beings as well, and they are extremely difficult to be degraded under routine conditions due to their high solubility and stability in the aquatic environment [3–10]. Years of research have found that catalysis is one of the most brilliant techniques to remove these organic compounds [3]. Nevertheless, such an eco-friendly technique can hardly proceed in the absence of a catalyst. Thus, developing a catalyst with high performance is of great importance for such a procedure.

In this regard, bimetallic alloy nanocatalysts have been proved to be efficient in accelerating the catalytic reaction, owing to their superior catalytic capacity over their monometallic counterparts derived from the change of electronic states of metals [11, 12]. Moreover, it is believed that the difference in work function may induce electron transfer between each component contributing to a prominent synergistic effect for catalysis [13]. Ni-based nanocatalysts, especially the Ni-noble metal alloy nanocatalysts with high catalytic efficiency were prepared and used in catalytic reduction or catalytic degradation dyes and nitroaromatic [11, 14–18]. On one hand, integration of earth-abundant Ni with noble metal can

reduce the cost to a certain extent; on the other hand, the magnetism of Ni is beneficial to the recovery of these catalysts. While, it is hard to keep small size for Ni-based alloy nanocatalysts, as they tend to aggregate due to its magnetism and high surface energy, leading to significant performance cost and lifetime. Thus, conquering the aggregation of Ni-based alloy nanocatalysts is still a puzzle.

Loading nanocatalysts onto all kinds of supports is proven to be an accessible method for controlling the size, ameliorating the dispersity and stability of nanocatalysts, especially the graphene and its derivative reduced graphene oxide (rGO) with large surface area, high conductivity, and easy surface functionalization [19, 20] What is more, the graphene/reduced graphene oxide supports have been reported to stimulate catalytic activity, permanence, poisoning tolerance, selectivity of metal nanoparticles loaded on them [21, 22]. All the above merits of graphene or rGO make it an ideal carrier for Ni-based alloy nanoparticles.

Thus, in present work, Ag-Ni alloy nanoparticles were in-situ anchored onto rGO surface homogeneously via a one-step co-reduction procedure with L-ascorbic acid as reducing agent. The detailed structure and morphology of the prepared Ag-Ni/rGO nanocomposite were characterized. The obtained products were used as catalysts in catalytic reduction of 4-nitrophenol and methylene blue. The catalytic performance of Ag-Ni/rGO is much superior to the reported alloy-decorated rGO nanocatalysts.

2 Materials and methods

2.1 Materials

Natural graphite powder was purchased from XF Nano (Nanjing, China); ammonia ($NH_3.H_2O$), potassium permanganate ($KMnO_4$), sodium nitrate ($NaNO_3$), hydrogen peroxide (H_2O_2, 30% in water), silver nitrate ($AgNO_3$), nickel chloride ($NiCl_2 \cdot 6H_2O$), sodium borohydride ($NaBH_4$), sulfuric acid (H_2SO_4, 98%), hydrochloric acid (HCl, 37%), L-ascorbic acid, 4-nitrophenol, and methylene blue of analytical purity were purchased from Sinopharm Chemical Reagent Co. Ltd. (Shanghai, China). Deionized (DI) water of 18.2 MΩ was used throughout the experiments.

2.2 Synthesis of Ag-Ni/rGO nanocomposite

Graphene oxide (GO) was synthesized via modified Hummers method as earlier reported [23, 24]. The GO powder was obtained by freeze-drying the obtained brown slurry.

The detailed steps for preparing Ag-Ni/rGO nanocomposite are displayed in Fig. 1 and described as follows: 15 mg GO powder was added into 30 mL DI water under continuous sonication for 30 min to form GO solution. Then, 200 μL of ammonia was added to the above GO solution under consecutive stirring. Subsequently, $AgNO_3$ aqueous solution (5 mL, 0.15 mol/L) and $NiCl_2 \cdot 6H_2O$ aqueous solution (5 mL, 0.15 mol/L) was mixed and then added to the above GO solution dropwise. The resultant mixture
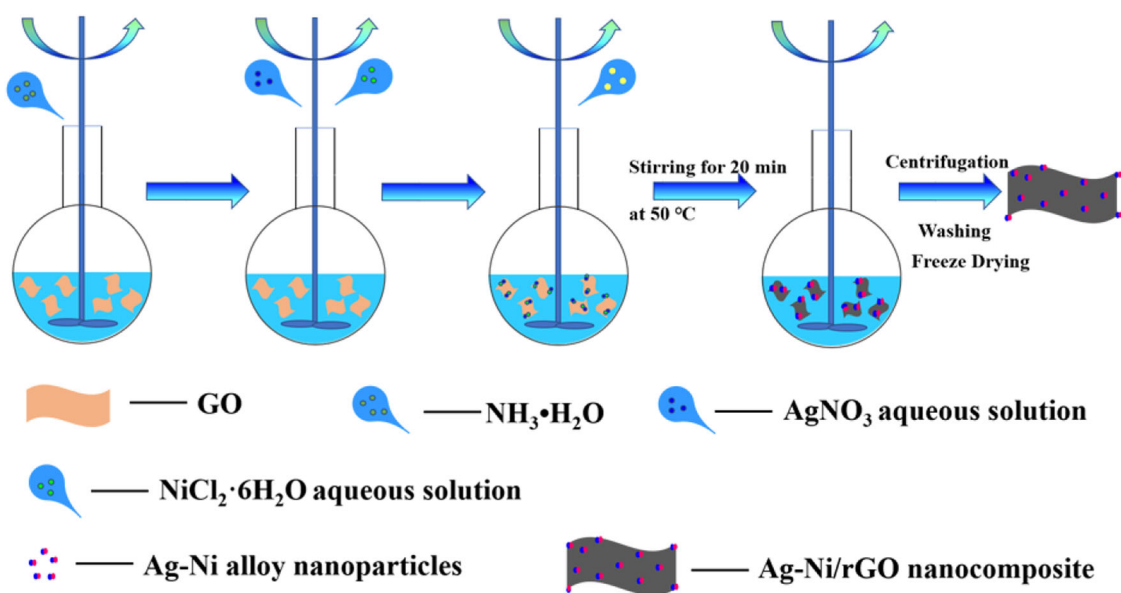

Fig. 1 Diagram of the synthesis procedure of Ag-Ni/rGO

was stirred for 1 h at room temperature (RT), and then 10 mL of L-ascorbic acid aqueous solution (1.14 mol/L) was added. The resultant system was heated to 50°C and reacted for 20 min. After cooling to RT, the obtained black product was centrifuged, washed with DI water, and then freeze-dried for use. Ag/rGO and Ni/rGO were prepared without adding $NiCl_2·6H_2O$ and $AgNO_3$ followed the same procedure.

2.3 Catalytic performance measurements

The catalytic performance tests of Ag-Ni/rGO were carried out by following steps.

Fresh $NaBH_4$ solution (5 mL, 0.3 M) was first added into 4-nitrophenol solution (50 mL, 0.1 mM) under stirring. Then 2 mg of Ag-Ni/rGO was introduced into the mixture to trigger the reaction. A certain amount of the above mixture was extracted at constant time intervals and monitored via UV-vis spectrophotometer from 200 nm to 600 nm. And all these operations were implemented at RT. The catalytic ability of Ag/rGO, Ni/rGO, and rGO were investigated following the same procedure. The above steps were also repeated to study the catalytic degradation of methylene blue (MB). Just the MB solution concentration of was set as 0.25 mM.

To investigate the recyclability of Ag-Ni/rGO, the catalysts were separated from the catalytic reaction system magnetically, and then used in the next round of reaction.

2.4 Characterization

Bruker AXS D8 Advance X-ray diffractometer was used to obtain XRD patterns of the samples. The morphology and crystal structure of the samples were examined by Transmission electron microscope (JEOL JEM 2100). Fourier transforms infrared (FTIR) spectra of the obtained samples were recorded by Nicolet Model 6700 spectrometer. Raman spectra of GO and Ag-Ni/rGO were acquired by HORIBA Scientific LabRAM HR Evolution Raman spectrometer. LakeShore 7404 was utilized to acquire magnetic hysteresis loops. The surface chemical state of GO and Ag-Ni/rGO was analyzed via Thermo Scientific K-alpha photoelectron spectrophotometer. All the UV-vis absorption spectra were recorded by Shimadzu UV-2600 spectrophotometer.

3 Results and discussion

3.1 Structural and morphology characterization

In the present work, the Ag-Ni alloy nanoparticles were in-situ anchored onto rGO sheets via the co-reduction of $AgNO_3$, $NiCl_2$, and GO with L-ascorbic acid working as a reductant. As the Ag^+ and Ni^{2+} was added into the GO solution, these metal ions would be attached onto GO surface via the electrostatic interaction between these positively charged ions and surface oxygenic groups with negative charge and then were reduced to their metallic state along with the adding of L-ascorbic acid. In the meantime, GO was reduced to rGO. Obviously, no surfactant participated in the synthesis process, thus the Ag-Ni alloy nanoparticles anchored on rGO were naked, which helps a lot in improving the catalytic capacity of Ag-Ni/rGO.

The crystallographic structures of the resulted specimens were characterized by XRD with GO XRD pattern as reference. As depicted in Fig. 2a, both of the XRD patterns of Ag/rGO and Ni/rGO show the characteristic diffraction peaks of face-centered cubic structure of Ag (JCPDS NO. 04-0783) and Ni (JCPDS NO. 04-0805). As for the Ag-Ni/rGO XRD pattern, distinct diffraction peaks of Ag (111), Ag (200), Ag (220), Ag (311), Ag (222), and Ni (200) emerged. It is quite a coincidence that these diffraction peaks of Ag (200) and Ag (311) belonging to Ag-Ni/rGO emerged almost between those of Ag/rGO, Ni/rGO, which is a hint of the generation of Ag-Ni alloy nanoparticles in the product [12, 22, 25]. The diffraction peaks of Ni (111)

Fig. 2 XRD pattern (**a**) and FTIR spectra (**b**) of GO, Ni/rGO, Ag/rGO, and Ag-Ni/rGO
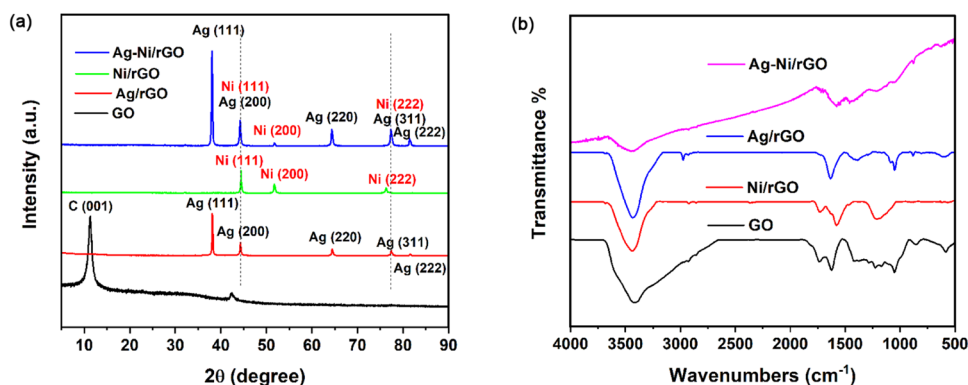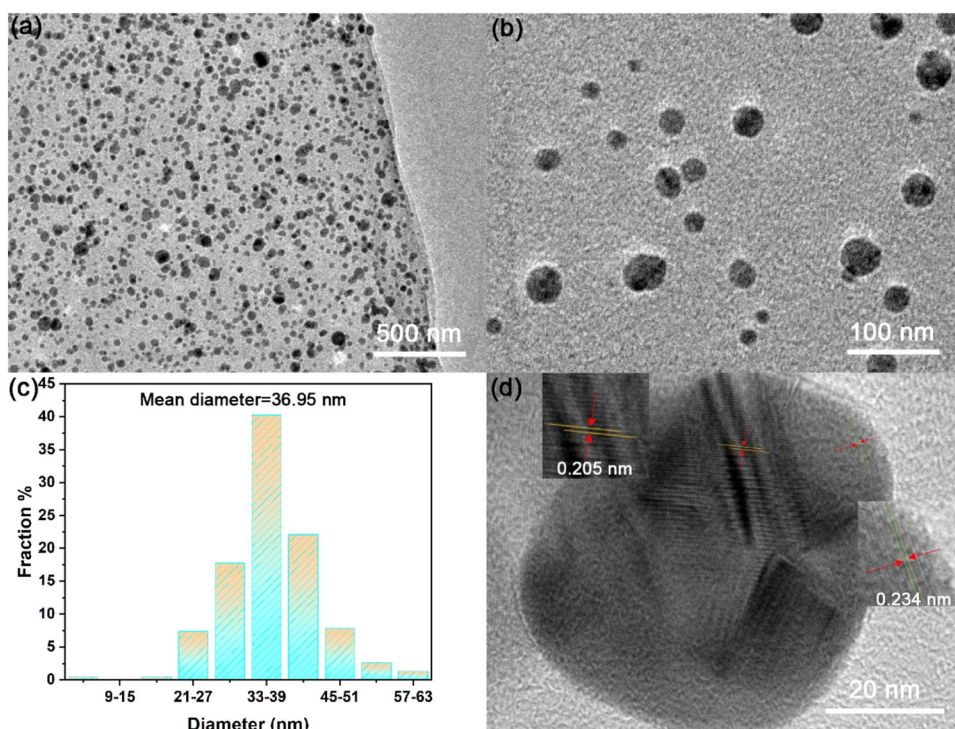
Fig. 3 a, **b** TEM images of Ag-Ni/rGO; **c** is bar diagram of Ag-Ni alloy nanoparticles in a size distribution; **d** HRTEM image of Ag-Ni/rGO

and Ni (222) should be covered by the Ag (200) and Ag (311) as previously reported [26]. Besides, the (002) crystallographic facet derived from the stacked rGO sheets did not appear in the XRD pattern of Ag/rGO, Ni/rGO, and Ag-Ni/rGO ascribed to the anchored nanoparticles impede the restacking of rGO sheets effectively [24], and the vanish of GO (001) crystallographic facet in the XRD patterns of the obtained nanocomposites suggesting the reduction of GO. No peaks attributed to impurity oxides could be detected in the aforementioned nanocomposites because of the protection of rGO sheets.

FTIR was further used to characterized the as-prepared samples. As the FTIR spectra in Fig. 2b showed, the peaks of oxygenic groups such as $C = O$ stretching mode ($1736\,cm^{-1}$), O-H deformation mode of C-OH ($1411\,cm^{-1}$), C-O stretching vibration of C-OH and C-O stretching vibration of epoxy groups ($1223\,cm^{-1}$) can be obviously detected in GO FTIR spectrum [17]. All of these peaks of oxygenic groups fade or even disappear for Ag/rGO, Ni/rGO, and Ag-Ni/rGO, suggesting GO suffered from a deoxygenation process during the formation of Ag/rGO, Ni/rGO, and Ag-Ni/rGO nanocomposite. Meanwhile, the decrease and disappearance of oxygenic groups peaks indicate the Ag, Ni, and Ag-Ni alloy nanoparticles were in-situ anchored onto rGO via the oxygenic groups which are likely to help in improving the dispersion of metal nanoparticles and enhancing the catalytic capacity of the resulting samples.

To acquire complete information about the size and morphology and further confirm the alloy structure of Ag-Ni nanoparticles in Ag-Ni /rGO nanocomposite, TEM and HRTEM were performed. As displayed in Figs. 3a and b, the Ag-Ni alloy nanoparticles are scattered homogeneously on the surface of rGO with no visible aggregation, and no unsupported nanoparticles can be detected. The mean size of the Ag-Ni alloy nanoparticles is 36.95 nm with a relatively narrow size distribution as illustrated in Fig. 3c. The good dispersion and relatively small size of Ag-Ni alloy nanoparticles implying the rGO is not only an ideal supporter but also an excellent dispersing agent for Ag-Ni alloy nanoparticles. Figure 3d displays the HRTEM image of Ag-Ni nanoparticle decorated on rGO. The visible lattice spacing of 0.205 nm can be attributed to the (111) plane of fcc Ni [18] and the displayed lattice spacing of 0.234 nm ascribing to the (111) plane of fcc Ag [26, 27] revealing the crystal nature of Ag-Ni alloy. The estimated lattice spacing for Ag-Ni nanoparticle shown in Fig. 2d do not match well with the reported Ni and Ag [14, 28]. This minor difference in lattice spacing may originated from the alloying of Ag and Ni.

The X-ray photoelectron spectroscopy (XPS) results shown in Fig. 4a-e depict the surface chemical state of GO and Ag-Ni/rGO nanocomposite and binding energies of the metals. Comparing with the XPS survey spectrum of GO, there are Ni 2p peak and Ag 3d peak emerged in the XPS that of Ag-Ni/rGO nanocomposite as displayed in Fig. 4a, confirming the co-existence of Ni and Ag species in the prepared Ag-Ni/rGO. And the surface atomic ratio (Ag: Ni) obtained from Fig. 4a is determined to be 53:48, which is close to the initial precursor (Ag^+: Ni^{2+}=1:1). Moreover, it

Fig. 4 **a** XPS spectra of GO and Ag-Ni/rGO; **b**, **c** high-resolution C1s spectra of GO and Ag-Ni/rGO; **d** Ag 3d spectrum of Ag-Ni/rGO; **e** Ni 2p spectrum of Ag-Ni/rGO; **f** Raman spectra of GO and Ag-Ni/rGO
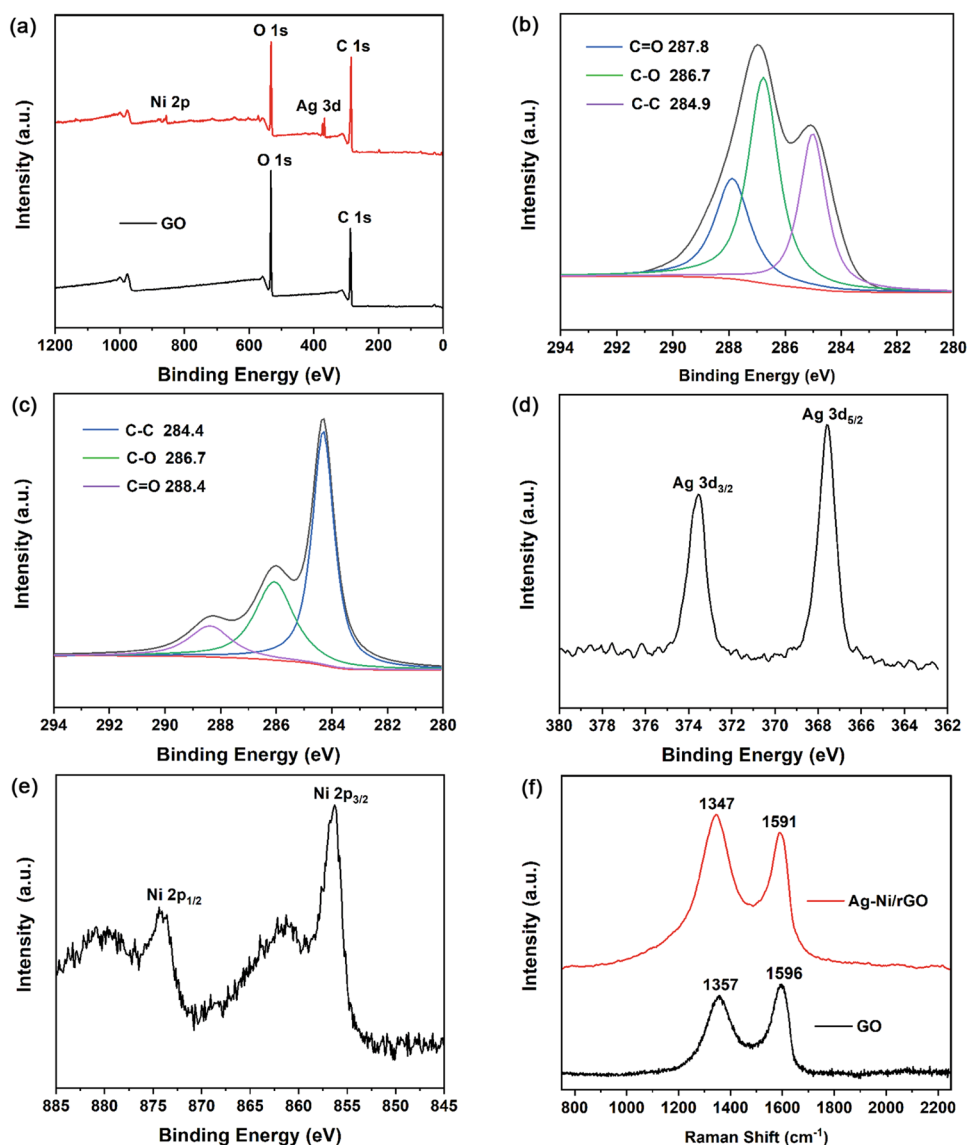

can be clearly detected that the relative intensity ratio of C/O of Ag-Ni/rGO is stronger than the one in GO, verifying the GO was reduced into rGO in prepared Ag-Ni/rGO. The C1s spectra of GO (Fig. 4(b)) can be fitted into three peaks located at 284.9 eV (C–C), 286.7 eV (C–O), and 287.8 eV (C=O). The C1s high-resolution XPS spectrum of Ag-Ni/rGO (Fig. 4c) displayed three characteristic peaks centered at 284.4 eV (C–C), 286.7 eV (C–O), and 288.4 eV (C=O). In comparison to GO, the peak location of C=O increased by 0.6 eV, the peak location of C-O showed no change, illustrating the Ag-Ni alloy nanoparticles were chemically bonded to rGO surface via C=O group [29, 30]; the peak location of C-C decreased by 0.5 eV, which may result from the formation of more numerous of small sp^2 domains during the reaction. Besides, the relative peak areas of C-O and C=O reduced a lot after the decoration of Ag-Ni alloy, this phenomenon indicates the GO was reduced to some extent.

These two peaks centered at 374.4 eV and 368.4 eV in Fig. 4d indicated the presence of metallic Ag in the Ag-Ni/rGO [24]. The detailed spectrum of Ni2p displayed two peaks at 856.6 eV and 874.1 eV as shown in Fig. 4f, which can be ascribed to the spin-orbit splitting of Ni2p$_{3/2}$ and Ni2p$_{1/2}$. What is noteworthy is that the binding energy for Ag species and Ni species in Ag-Ni/rGO both show distinct difference from those of pure metallic Ag (374.6 eV and 368.6 eV) pure metallic Ni (853.2 eV and 870.9 eV) as a result of the electronic interactions derived from electron-negative difference between metallic Ag0 and Ni0 [31], confirming the formation of Ag-Ni alloy and the change in surface electronic structure between alloy compositions [32].

Raman spectra were acquired to investigate the carbon structure changes form GO to Ag-Ni/rGO. Figure 4(f) displays the Raman spectra of Ag-Ni/rGO and GO. Both of the specimens exhibit two apparent peaks of D band ascribing

Fig. 5 a–c UV-vis spectra of the reduction of 4-nitrophenol by NaBH$_4$ with Ag-Ni/rGO, Ag/rGO, and Ni/rGO as catalyst, respectively; **d** Plots of ln(C/C$_0$) against time
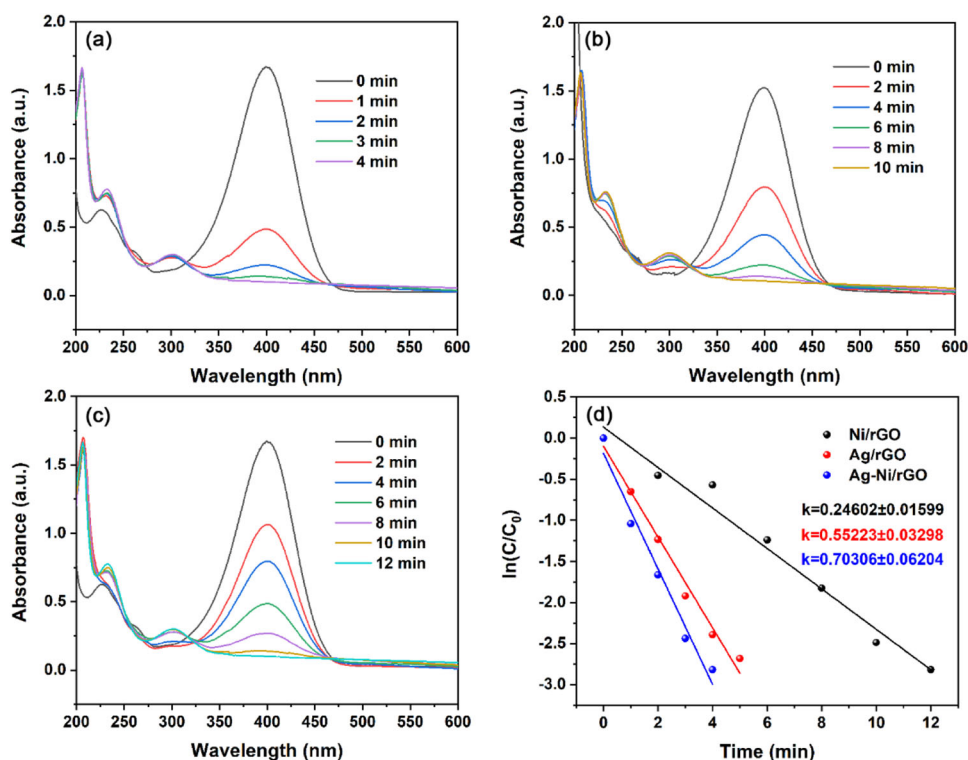
to the breathing mode of κ-point phonons brought out by the defects and disordered structure and G band corresponding to the in-plane vibration of sp^2-C atoms arranged in the graphitic lattice, respectively [33, 34]. In comparison with GO, it can be detected that the D band of Ag-Ni/rGO moves to 1357 cm^{-1} and G band of Ag-Ni/rGO moves to 1591 cm^{-1}, implying electron transmission occurred between Ag-Ni nanoparticles and rGO. As intensity ratio of D and G bands (I$_D$/I$_G$) which is considered as an indicator of disorder parameter of graphitic displays an increase from 1.14 for GO to 1.41 for Ag-Ni/rGO, indicating the generation of more structural defects and exposed edges, and GO was reduced into rGO during the synthesis procedure [26]. The introduction of more structural defects and exposed edges would contribute to the increase of surface area of resulted rGO, and then improve the catalytic performance of Ag-Ni/rGO.

3.2 Catalytic performance of Ag-Ni/rGO

3.2.1 Catalytic reduction of 4-nitrophenol

The prepared Ag-Ni/rGO nanocomposite was first utilized to catalyze the hydrogenation reduction of nocuous dye intermediates 4-nitrophenol [35]. As shown in Fig. 5a, with the presence of NaBH$_4$, a distinct peak belonging to 4-nitrophenolate ion emerged at 400 nm [17]. With the adding of Ag-Ni/rGO, the peak of 4-nitrophenolate ion weakened

gradually along with a newborn peak ascribing to 4-aminophenol strengthened at about 300 nm as the reaction time goes on, which is an indicator of the transformation of 4-nitrophenol into 4-aminophenol [7, 36]. The reaction ended as the peak at 400 nm disappeared in the fourth minute. Such a short reaction time, implying the Ag-Ni/rGO nanocatalyst possesses outstanding catalytic performance. It is worth noting that three isobestic point located at 315 nm, 254 nm, and 274 nm can be observed in Fig. 5a, suggesting no byproduct generated during the catalytic reaction [37].

In order to study the catalytic performance of bimetallic Ag-Ni/RGO more deeply, the catalytic capacity of monometallic Ag/rGO and Ni/rGO were studied for comparison. Parallel tests were performed under the same conditions and corresponding results are displayed in Figs. 5b and c, the relevant reaction finished in 10 min for Ag/rGO and 12 min for Ni/rGO, which are both longer than that for Ag-Ni/rGO. Therefore, the catalytic performance of bimetallic Ag-Ni/rGO outperforms the monometallic counterparts.

As the reductions of 4-nitrophenol were conducted with superfluous NaBH$_4$, it is concluded that these above reactions follow the pseudo-first-order kinetics as reported [24, 38]. Thus, the plots of ln(C/C$_0$) against time t were obtained and depicted in Fig. 5d. Good linear correlations can be observed, confirming all these above reductions followed the pseudo-first-order kinetics rule. The apparent rate constant (k) of Ag-Ni/rGO estimated based on the plot shown in Fig. 5d is

$0.70306 \pm 0.06204 \, \text{min}^{-1}$, surpassing $0.55223 \pm 0.03298 \, \text{min}^{-1}$ of Ag/rGO and $0.24602 \pm 0.01599 \, \text{min}^{-1}$ of Ni/rGO, further confirming the catalytic activity of Ag-Ni/rGO is better than that of the corresponding monometallic counterparts. Furthermore, the k of Ag-Ni/rGO also exceeds the k of the other analogous catalysts in reported works displayed in Table 1, suggesting the advantageous catalytic activity of Ag-Ni/rGO once again.

Based on the above catalytic performance test results, it is logical to speculate that the dramatically enhanced catalytic performance of Ag-Ni/rGO is derived from the synergistic effects of Ag and Ni component in Ag-Ni/rGO. As the catalytic reaction proceeds, the BH_4^- would be adsorbed onto the surface of the heterogenous Ag-Ni/rGO catalyst and delivery active hydrogen species to the surface of Ag-Ni alloy

Table 1 The reported reaction rate constant (k) of graphene-based nanocatalysts for the catalytic reduction of 4-nitrophenol

| Catalyst	k (min^{-1})	Reference
Ag-Ni/rGO	0.70306 ± 0.06204	This work
RGO-Ni$_{0.25}$Co$_{0.75}$	0.00773 ± 0.00013	[32]
RGO-Ni$_{0.50}$Co$_{0.50}$	0.09322 ± 0.00378	[32]
RGO-Ni$_{0.75}$Co$_{0.25}$	0.02906 ± 0.0006	[32]
Pd-Ni/rGO	0.160	[15]
Pd-Ni/C	0.142	[15]
Ag-Pd-PDA/rGO	0.324	[48]
Pt-Au dendrites/rGO	0.228	[39]
Fe@Au-ATPGO	0.084	[49]
AuPt@Au NCs/rGO	0.522	[50]
Ni@PtNi/rGO	0.270	[51]
Ag@Au/rGO	0.3216	[52]
Ag@Pd/rGO	0.5202	[52]
PdAg-Gr	0.0738 ± 0.0012	[22]
Pt1Co3Ncs/N-rGO	0.2802	[53]
RGO-Ni-Ag-6h	0.662	[17]
Ag-Au/rGO	0.2082	[26]
Pd-Ag/rGO	0.2413	[40]

nanoparticles [39]. At the same time, 4-nitrophenol would also be enriched to the surface of Ag-Ni/rGO catalyst by the virtue of large specific area of rGO supporter and the π-π stacking interactions exist between rGO and π-riched 4-nitrophenol [24, 38]. Thus, resulting the transformation of 4-nitrophenol to 4-aminiphenol. During the reaction, the difference in work between Ag (4.26 eV) and Ni (4.6) would induce the electron transfer from Ag to Ni, forming an electron-rich regions [17, 40–43]. As a plenty of Ag-Ni alloy nanoparticles were decorated on rGO, abundant of electron-rich regions existed in Ag-Ni/rGO, which facilitated the enrichment of 4-nitrophenol and contributed the digestion of electrons by 4-nitrophenol, resulting the catalytic performance improvement of Ag-Ni/rGO. As the surface of Ag-Ni alloy nanoparticles on rGO are naked, all the Ag-Ni alloy nanoparticles surfaces are available for the catalysis process and contributory to the enhancement of Ag-Ni/rGO catalytic capacity, as well.

3.2.2 Catalytic degradation of MB

Organic pollutant with high toxicity and non-biodegradable property are reported to have negative effect on the aquatic environment and the health of human beings and animals [44–46]. As a representative organic pollutant, MB was chosen as model to further test the catalytic degradation performance of the Ag-Ni/rGO sample. The UV-vis spectra of the MB degradation detected in the range of 450–800 nm is depicted in Fig. 6a. Upon adding of Ag-Ni/rGO, the characteristic peaks of MB decreased immediately and displayed no change after 7 min. The degradation rate is determined to be 82.24%. Good linear correlation with a correlation coefficient of 0.9883can be observed in Fig. 6b, indicating pseudo-first-order kinetics law was followed. The k determined from the plot shown in Fig. 6b is $0.24837 \pm 0.01023 \, \text{min}^{-1}$, outperforming the other reported catalysts listed in Table 2, further verifying the outstanding catalytic capacity of Ag-Ni/rGO.

Owing to the enormous difference in in the redox potential, the redox reaction cannot happen between $NaBH_4$

Fig. 6 a UV-vis spectra of the reduction of MB and b Plots of $\ln(C/C_0)$ against time with Ag-Ni/rGO as catalyst
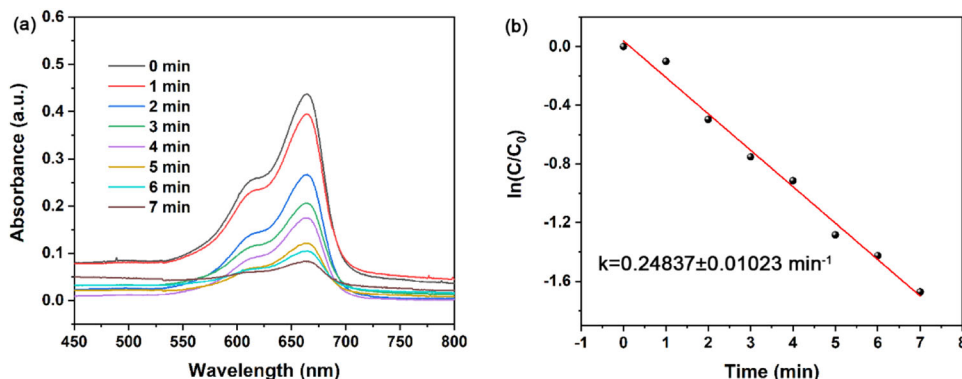
and dyes under conventional conditions [47]. With the presence of Ag-Ni/rGO catalyst, the intermediate redox potential of metal nanoparticles makes them can work as transmitter for electrons transmission from $NaBH_4$ to MB, facilitating the redox reaction. Therefore, during the catalytic reduction of MB, the anchored Ag-Ni nanoparticles with electron-rich regions can serve as the electron "relay station" and delivery electron to the adsorbed MB, leading to transformation of MB into the colorless and nontoxic leuco methylene blue and amines [38]. The rGO substrate with a large area helped in enriching MB to the surface of Ag-Ni/rGO, accelerating the reduction of MB.

3.2.3 Magnetic property and recyclability

The existence of Ni element in the Ag-Ni/rGO may make it magnetic. Therefore, the magnetic properties of Ni/rGO and Ag-Ni/rGO were investigated and the corresponding magnetic hysteresis loops are shown in Fig. 7. Both of the hysteresis curves of Ag-Ni/rGO and Ni/rGO display the representative form of S-like curve, revealing the ferromagnetic nature of the obtained samples [32] and further suggesting the formation of Ni species within the rGO matrix. The magnetization (Ms), remanence (Mr), remanence-to-saturation ratio (Mr/Ms) and coercivity (Hc) of Ag-Ni/rGO are listed in Table 3. As shown in Table 3, the saturation magnetization value of Ag-Ni/rGO

was determined to be 18.29. emu/g, which is lower than 30.48 emu/g of Ni/rGO, as a result of the existence of non-magnetic Ag [17]. As the public known, it is difficult to recycle the nanocatalyst due to the small size. However, benefiting from the considerable magnetic of the resultant Ag-Ni/rGO, it can be separated by external magnet from the liquid media with ease as shown in the inset of Fig. 7b, then used in the next cycle.

To further evaluate recyclability and catalytic performance stability, the catalytic reduction of 4-nitrophenol into 4-aminophenol was repeated. As the recyclability test results shows in Fig. 8(a), the conversion can still maintain around 95.2% after ten cycles, verifying the Ag-Ni/rGO has high catalytic stability. The loss of conversion may because of the inevitable mass loss of the as-prepared catalyst. Little change can be observed in the XRD patterns (Fig. 8b) of fresh Ag-Ni/rGO and the one use for ten cycles, confirming the high structural stability of Ag-Ni/rGO catalyst. And from the TEM images shown in Fig. 8c, d, the morphology of the as-prepared Ag-Ni/rGO catalyst changed little in the recycling process. In conclusion, the Ag-Ni/rGO exhibited excellent catalytic stability.

4 Conclusions

To sum up, a simple co-reduction strategy was proposed for preparing Ag-Ni/rGO nanocomposite with L-ascorbic acid as reductant. The Ag-Ni alloy nanoparticles in resultant products showed relatively small size and almost no agglomeration with the rGO sheets work as supporter and dispersing agent. The resultant Ag-Ni/rGO nanocomposite

Table 2 The reported reaction rate constant (k) of graphene-based nanocatalysts for the catalytic degradation of MB

Catalyst	k (min^{-1})	Reference
Ag-Ni/rGO	0.24837 ± 0.01023	This work
IO/GA-RPB	0.0926 min^{-1}	[2]
Au/3D-graphene	0.0238 min^{-1}	[54]
Pd/3D-graphene	0.0689 min^{-1}	[55]
Ag/rGO	0.01398	[56]
GO-AgNPs	0.034	[57]
Au NPs/MCNSs	0.1967	[58]

Table 3 The magnetic data of Ni/rGO and Ag-Ni/rGO

Samples	Ms (emu/g)	Mr (emu/g)	Mr/Ms	Hc (Oe)
Ni/rGO	30.48	2.94	0.096	97.58
Ag-Ni/rGO	18.29	1.87	0.102	87.09

Fig. 7 Hysteresis loops of a Ni/rGO and b Ag-Ni/rGO
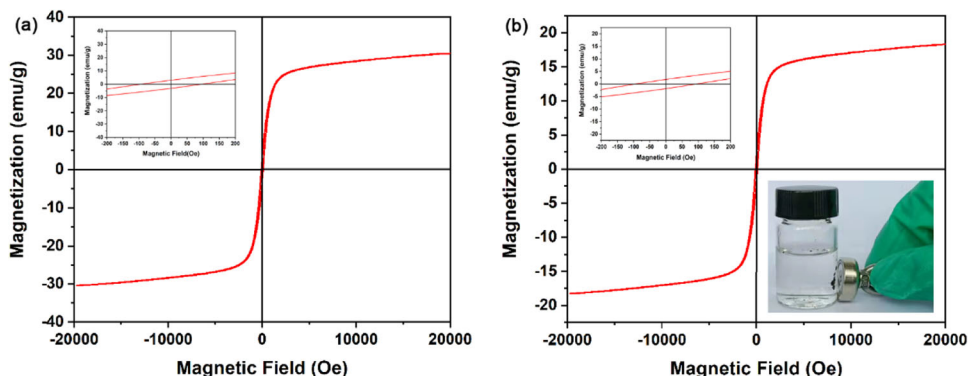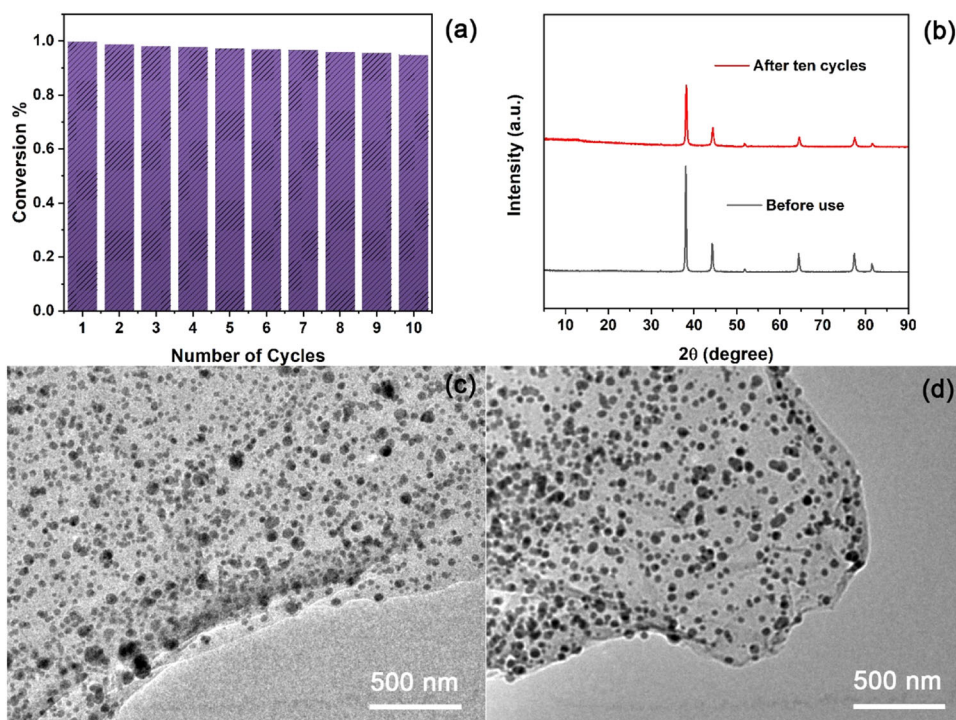
Fig. 8 a Stability measurement of Ag-Ni/rGO; **b** The XRD patterns of Ag-Ni/rGO before use and after recycling test; **c**, **d** The TEM images of Ag-Ni/rGO before use and after recycling test

exhibited superior catalytic capacity towards the reduction reaction of 4-nitrophenol and methylene blue. Resulting from the magnetism of Ag-Ni/rGO, it could be removed from the catalytic reduction system easily and reused without apparent loss in catalytic performance. It concluded that the naked surface, electron transfer between Ag-Ni nanoparticles and rGO and that originated from the work function difference between Ag and Ni of the Ag-Ni bimetallic nanoparticles facilitate the relevant reduction reactions. This work provides a facile case for acquiring high-performance catalyst for catalysis application.

Author Contributions All authors contributed to the study's conception and design. Material preparation, data collection, and analysis were performed by JP, ZM, HZ, YY, JZ, SG, and HP. The first draft of the manuscript was written by Xing-Wei Han and all authors commented on previous versions of the manuscript.

Compliance with ethical standards

References

1. Shi H, Chen X, Liu K, Ding X, Liu W, Xu M (2020) Heterogeneous Fenton ferroferric oxide-reduced graphene oxide-based composite microjets for efficient organic dye degradation. J Colloid Inter Sci 572:39–47

2. Zhao Z, Wang Z, Wang D, Wang JX, Foster NR, Pu Y, Chen JF (2018) Preparation of 3D graphene/iron oxides aerogels based on high-gravity intensified reactive precipitation and their applications for photo-Fenton reaction. Chem Eng Process 129:77–83

3. Nasrollahzadeh M, Atarod M, Jaleh B, Gandomi M (2016) In situ green synthesis of Ag nanoparticles on graphene oxide/TiO$_2$ nanocomposite and their catalytic activity for the reduction of 4-nitrophenol, Congo red, and methylene blue. Ceram Int 42:8587–8596

4. Le VT, Doan VD, V Tran A, Lea HS, Tran DL, Pham TM, Tran TH, Nguyen HT (2020) Cu/Fe$_3$O$_4$@carboxylate-rich carbon composite: One-pot synthesis, characterization, adsorption and photo-Fenton catalytic activities. Mater Res Bull 129:110913

5. Rout L, Kumar A, Dhaka RS, Reddy GN, Giri S, Dash P (2017) Bimetallic Au-Cu alloy nanoparticles on reduced graphene oxide support: synthesis, catalytic activity and investigation of synergistic effect by DFT analysis. Appl Catal A-Gen 538:107–122

6. de Barros MR, Bittencourt OR, Crocomo PZ, Mafra G, Carasek E, Magosso HA, Jost CL, Winiarski JP (2021) Adsorption of hazardous and noxious 4-nitrophenol by a silsesquioxane organic-inorganic hybrid material. J Sol-Gel Sci Technol 99:402–412

7. Patra AK, Dutta A, Bhaumik A (2010) Cu nanorods and nanospheres and their excellent catalytic activity in chemoselective reduction of nitrobenzenes. Catal Commun 11:651–655

8. Liu M, Liu X, Wang P, Zhang X (2021) N-doped three-dimensional graphene aerogel with a high loading of Ag particles as an efficient catalyst and antibacterial agent. Colloid Surf A 626:126886

9. Zhang Y, Li C, Liu X, Xu J, Yang X, Zhang (2021) Facile g-ray irradiation synthesis of Pt/GA nanocomposite for catalytic reduction of 4-nitrophenol. Green Energy Environ 6:734–742

10. Li P, Wang H, Jiang J, Cao Z, Yang J (2022) Rational design of metal/N-doped carbon nanocatalysts via sol-gel method for obtaining high catalytic activity toward reduction reactions of 4-nitrophenol and Rhodamine B. Appl Catal A-Gen 631:118479

11. Gao X, Zhao H, Liu Y, Ren Z, Lin C, Tao J, Zhai Y (2018) Facile synthesis of PdNiP/reduced graphene oxide nanocomposites for

catalytic reduction of 4-nitrophenol. Mater Chem Phys 222:391–397

12. Zhu XY, Lv ZS, Feng JJ, Yuan PX, Zhang L, Chen JR, Wang AJ (2018) Controlled fabrication of well-dispersed AgPd nanoclusters supported on reduced graphene oxide with highly enhanced catalytic properties towards 4-nitrophenol reduction. J Colloid Inter Sci 516:55–363

13. Chen H, Fan X, Ma J, Zhang G, Zhang F, Li Y (2014) Green route for microwave-assisted preparation of AuAg-alloy decorated graphene hybrids with superior 4-NP reduction catalytic activity. Ind Eng Chem Res 53:17976–17980

14. Zhang Z, Lu ZH, Chen X (2015) Ultrafine Ni-Pt alloy nanoparticles grown on graphene as highly efficient catalyst for complete hydrogen generation from hydrazine borane. ACS Sustain Chem Eng 3:1255–1261

15. Revathy TA, Dhanavel S, Sivaranjani T, Narayanan V, Maiyalagan T, Stephen A (2018) Highly active graphene-supported palladium-nickel alloy nanoparticles for catalytic reduction of 4-nitrophenol. Appl Surf Sci 449:764–771

16. Yang J, Shen X, Ji Z, Zhou H, Zhu G, Chen K (2014) In situ growth of hollow CuNi alloy nanoparticles on reduced graphene oxide nanosheets and their magnetic and catalytic properties. Appl Surf Sci 316:575–581

17. Li X, Ma Y, Yang Z, Huang D, Xu S, Wang T, Su Y, Hu N, Zhang Y (2017) In situ preparation of magnetic Ni-Au/graphene nanocomposites with electron enhanced catalytic performance. J Alloy Compd 706:377–386

18. Krishna R, Fernandes DM, Ventura J, Freire C, Titus E (2016) Novel synthesis of highly catalytic active Cu@Ni/RGO nanocomposite for efficient hydrogenation of 4-nitrophenol organic pollutant. Int J Hydrog Energ 41:11608–11615

19. Hanifah MFR, Jaafar J, Othman MHD, Ismail AF, Rahman MA, Yusof N, Aziz F, Rahman NA (2019) One-pot synthesis of efficient reduced graphene oxide supported binary Pt-Pd alloy nanoparticles as superior electro-catalyst and its electro-catalytic performance toward methanol electro-oxidation reaction in direct methanol fuel cell. J Alloy Compd 793:232–246

20. Hao X, Jiang Z, Tian X, Song C, Chen S, Hao X, Jiang ZJ (2020) Synthesis of ultrasmall, homogeneously distributed Ni$_3$Fe alloy nanoparticles on N-doped porous graphene as a bifunctional electrocatalyst for rechargeable flexible solid zinc-air batteries. ACS Appl Energy Mater 3:12148–12161

21. Bhowmik T, Kundu MK, Barman S (2016) Palladium nanoparticle-graphitic carbon nitride porous synergistic catalyst for hydrogen evolution/oxidation reactions over a broad range of pH and correlation of its catalytic activity with measured hydrogen binding energy. ACS Catal 6:1929–1941

22. Bhat SA, Rashid N, Rather MA, Pandit SA, Rather GM, Ingole PP, Bhat MA (2018) PdAg bimetallic nano alloy decorated graphene: a nanohybrid with unprecedented electrocatalytic, catalytic and sensing activity. ACS Appl Mater Inter 10:16376–16389

23. Hummers WS, Offman RE (1958) Preparation of graphitic oxide. J Am Chem Soc 80:1339–1339

24. Han XW, Pan H, Liu M (2020) In situ construction of reduced graphene oxide supported Ag nanoneedles heterogenous nanostructures with superior catalytic activity for 4-nitrophenol. Colloids Surf A 600:124929

25. Liu Q, He YM, Weng X, Wang AJ, Yuan PX, Fang KM, Feng JJ (2018) One-pot aqueous fabrication of reduced graphene oxide supported porous PtAg alloy nanoflowers to greatly boost catalytic performances for oxygen reduction and hydrogen evolution. J Colloid Inter Sci 513:455–463

26. Hareesh K, Joshi RP, Sunitha DV, Bhoraskar VN, Dhole SD (2016) Anchoring of Ag-Au alloy nanoparticles on reduced graphene oxide sheets for the reduction of 4-nitrophenol. Appl Surf Sci 389:1050–1055

27. Sahoo PK, Kumar N, Thiyagarajan S, Thakur D, Panda HS (2018) Freeze-casting of multifunctional cellular 3D-graphene/Ag nanocomposites: synergistically affect supercapacitor, catalytic and antibacterial properties. ACS Sustain Chem Eng 6:7475–7487

28. Kellici S, Acord J, Vaughn A, Power NP, Morgan DJ, Heil T, Facq SP, Lampronti GI (2016) Calixarene assisted rapid synthesis of silver-graphene nanocomposites with enhanced antibacterial activity. ACS Appl Mater Inter 8:19038–19046

29. Zhang F, Song Y, Song S, Zhang R, Hou W (2015) Synthesis of magnetite-graphene oxide-layered double hydroxide composites and applications for the removal of Pb (II) and 2,4-dichlorophenoxyacetic acid from aqueous solutions. ACS Appl Mater Inter 7:7251–7263

30. Zhang B, Hu R, Sun D, Wu T, Li Y (2018) Fabrication of magnetite-graphene oxide/MgAl-layered double hydroxide composites for efficient removal of emulsified oils from various oil-in-water emulsions. J Chem Eng Data 63:4689–4702

31. Dhanda R, Kidwai M (2015) Reduced graphene oxide supported Ag$_x$Ni$_{100-x}$ alloy nanoparticles: a highly active and reusable catalyst for the reduction of nitroarenes. J Mater Chem A 3:19563–19574

32. Bai S, Shen X, Zhu G, Li M, Xi H, Chen K (2012) In situ growth of Ni$_x$Co$_{100-x}$ nanoparticles on reduced graphene oxide nanosheets and their magnetic and catalytic properties. ACS Appl Mater Inter 4:2378–2386

33. Zheng F, Luk SY, Kwong TL, Yung KF (2016) Synthesis of hollow PtAg alloy nanospheres with excellent electrocatalytic performances towards methanol and formic acid oxidations. RSC Adv 6:44902–44907

34. Vilian ATZ, Choe SR, Giribabu K, Jang S-C, Roh C, Huh YS, Han Y-K (2017) Pd nanospheres decorated reduced graphene oxide with multifunctions: highly efficient catalytic reduction and ultrasensitive sensing of hazardous 4-nitrophenol pollutant. J Hazard Mater 333:54–62

35. Jaerger S, dos Santos A, Fernandes AN, Almeida CAP (2015) Removal of p-nitrophenol from aqueous solution using brazilian peat: kinetic and thermodynamic Studies. Water Air Soil Poll 226:236

36. Wu Y, Wen M, Wu Q, Fang H (2014) Ni/graphene nanostructure and its electron-enhanced catalytic action for hydrogenation reaction of nitrophenol. J Phys Chem C 118:6307–6313

37. Kong X, Sun Z, Chen M, Chen C, Chen Q (2013) Metal-free catalytic reduction of 4-nitrophenol to 4-aminophenol by N-doped graphene. Energy Environ Sci 6:3260–3266

38. Han X-W, Guo S, Li T, Peng J, Pan H (2022) Construction of Ag/3D-reduced graphene oxide nanocomposite with advanced capacity for 4-nitrophenol and methylene blue. Colloids Surf A 650:128688

39. Lv JJ, Wang AJ, Ma X, Xiang RY, Chen JR, Feng JJ (2015) One-pot synthesis of porous Pt-Au nanodendrites supported on reduced graphene oxide nanosheets toward catalytic reduction of 4-nitophenol. J Mater Chem A 3:290–296

40. Han R, Song X, Wang Q, Qi Y, Deng G, Zhang A, Wang Q, Chang F, Wu C, Cheng Y (2019) Microbial synthesis of graphene-supported highly-dispersed Pd-Ag bimetallic nanoparticles and its catalytic activity. J Chem Technol Biot 94:3375–3383

41. Wunder S, Polzer F, Lu Y, Mei Y, Ballauff M (2010) Kinetic features of the platinum-catalyzed hydrolysis of sodium borohydride from 11B NMR measurements. J Phys Chem C 114:8814–8820

42. Kovtunov KV, Barskiy DA, Salnikov OG, Burueva DB, Khudorozhkov AK, Bukhtiyarov AV, Prosvirin IP, Gerasimov EY, Bukhtiyarov VI, Koptyug IV (2015) Strong metal-support interactions for palladium supported on TiO$_2$ catalysts in the heterogeneous hydrogenation with parahydrogen. ChemCatChem 7:2581–2584

43. Li S, Guo S, Yang H, Gou G, Ren R, Li J, Dong Z, Jin J, Ma J (2014) Enhancing catalytic performance of Au catalysts by non-covalent functionalized graphene using functional ionic liquids. J Hazard Mater 270:11–17

44. Lim EB, Tran AV, Lee SW (2020) Comparative release kinetics of small drugs (ibuprofen and acetaminophen) from multi-functional mesoporous silica nanoparticles. J Mater Chem B 8:2096–2106

45. Luu TVH, Luu MD, Dao NN, Le VT, Nguyen HT, Doan VD (2021) Immobilization of C/Ce-codoped ZnO nanoparticles on multiwalled carbon nanotubes for enhancing their photocatalytic activity. J Disper Sci Technol 49:1311–1322

46. Tran VA, Tran NHT, Bach LG, Nguyen TD, Nguyen TT, Nguyen TT, Nguyen TAN, Vo TK, Vo TTT, Le VT (2020) Facile synthesis of propranolol and novel derivatives. J Chem 2020:9597426

47. Gupta N, Singh HP, Sharma RK (2021) Metal nanoparticles with high catalytic activity in degradation of methyl orange: an electron relay effect. J Mol Catal A Chem 335:248–252

48. Ghorbania NA, Namazi H (2019) Polydopamine-graphene/Ag-Pd nanocomposite as sustainable catalyst for reduction of nitrophenol compounds and dyes in environment. Mater Chem Phys 234:38–47

49. Gupta VK, Atar N, Yola ML, Ustundag Z, Uzun L (2014) A novel magnetic Fe@Au core-shell nanoparticles anchored graphene oxide recyclable nanocatalyst for the reduction of nitrophenol compounds. Water Res 48:210–217

50. Liu Q, Xu Y, Wang A, Feng J (2015) One-step melamine-assisted synthesis of graphene-supported AuPt@Au nanocrystals for enhanced catalytic reduction of p-nitrophenol. RSC Adv 5:96028–96033

51. Mei LP, Wang R, Song P, Feng JJ, Wang ZG, Chen JR, Wang AJ (2016) One-pot solvothermal synthesis of bimetallic yolk-shell Ni@PtNi nanocrystals supported on reduced graphene oxide and their excellent catalytic properties for p-nitrophenol reduction. N. J Chem 40:2315–2320

52. Liu CH, Chen XQ, Hu YF, Sham TK, Sun QJ, Chang JB, Gao X, Sun XH, Wang SD (2013) One-pot environmentally friendly approach toward highly catalytically active bimetal-nanoparticle-graphene hybrids. ACS Appl Mater Inter 5:5072–5079

53. Zhang XF, Zhu XY, Feng JJ, Wang AJ (2018) Solvothermal synthesis of N-doped graphene supported PtCo nanodendrites with highly catalytic activity for 4-nitrophenol reduction. Appl Surf Sci 428:798–808

54. Liu T, Cui Z, Liu Y, Ba X (2019) In-situ fabrication of ultrafine Pd supported on nitrogen-doped reduced graphene oxide via nitrogen glow discharge plasma for catalytic reduction of 4-nitrophenol. Appl Catal A-Gen 588:117278

55. Sahooa PK, Panigrahyc B, Thakurb D, Bahadurb D (2017) Ice-templating synthesis of macroporous noble metals/3Dgraphene nanocomposites: their fluorescence lifetime and catalytic study. N. J Chem 41:7861–7869

56. He C, Liu Z, Lu Y, Huang L, Yang Y (2016) Graphene-supported silver nanoparticles with high activities toward chemical catalytic reduction of methylene blue and electrocatalytic oxidation of hydrazine. Int J Electrochem Sci 11:9566–9574

57. Sreekanth TVM, Jung M-J, Eom I-Y (2016) Green synthesis of silver nanoparticles, decorated on graphene oxide nanosheets and their catalytic activity. Appl Surf Sci 361:102–106

58. Zuo W, Chen G, Chen F, Li S, Wang B (2016) Green synthesis and characterization of gold nanopartilces embedded into magnetic carbon nanocages and their high efficient degradation for methylene blue. RSC Adv 6:28774–28780